A&A 390, 633–647 (2002)
DOI: 10.1051/0004-6361:20020726

Astronomy & Astrophysics

Zeeman tomography of magnetic white dwarfs

I. Reconstruction of the field geometry from synthetic spectra

F. Euchner[1], S. Jordan[1,2,3], K. Beuermann[1], B. T. Gänsicke[1], and F. V. Hessman[1]

[1] Universitäts-Sternwarte Göttingen, Geismarlandstr. 11, 37083 Göttingen, Germany
[2] Institut für Astronomie und Astrophysik, Universität Kiel, 24098 Kiel, Germany
[3] Institut für Astronomie und Astrophysik, Universität Tübingen, Sand 1, 72076 Tübingen, Germany

Received 7 February 2002 / Accepted 15 May 2002

Abstract. We have computed optical Zeeman spectra of magnetic white dwarfs for field strengths between 10 and 200 MG and effective temperatures between 8000 and 40 000 K. They form a database containing 20 628 sets of flux and circular polarization spectra. A least-squares optimization code based on an evolutionary strategy can recover relatively complex magnetic field topologies from phase-resolved synthetic Zeeman spectra of rotating magnetic white dwarfs. We consider dipole and quadrupole components which are non-aligned and shifted off-centre. The model geometries include stars with a single high-field spot and with two spots separated by ∼90°. The accuracy of the recovered field structure increases with the signal-to-noise ratio of the input spectra and is significantly improved if circular polarization spectra are included in addition to flux spectra. We discuss the strategies proposed so far to unravel the field geometries of magnetic white dwarfs.

Key words. white dwarfs – stars: magnetic fields – stars: atmospheres – polarization

1. Introduction

About 3% of all white dwarfs have strong magnetic fields between 10^6 and 10^9 Gauss (Wickramasinghe & Ferrario 2000; Jordan 2001). In many of these magnetic white dwarfs (MWDs), the surface field geometries deviate from simple centred dipoles. This holds for isolated MWDs and for the MWDs in accreting close binaries (Wickramasinghe & Ferrario 2000; Schwope 1995). While higher modes are often thought to decay on timescales longer than the $\tau \gtrsim 10^{10}$ yr of the fundamental mode, Muslimov et al. (1995) showed that quadrupole or octupole components may survive via the Hall effect if an internal toroidal magnetic field component is present. Therefore, studies of the surface field structure provide clues on the internal field configuration and its influence on the evolution of MWDs.

The photospheric spectra of hydrogen-rich MWDs are characterized by broad absorption structures formed by the overlap of numerous components of the Balmer lines, shifted by hundreds or even thousands of Å from their zero-field positions by the linear and quadratic Zeeman effects. These shifts completely obliterate the Doppler shifts caused by rotation even in the most rapidly rotating MWDs. As a consequence, the Zeeman-Doppler imaging method devised for the analysis of rapidly rotating magnetically active main sequence stars (Semel 1989; Donati et al. 1989; Brown et al. 1991) is not applicable to MWDs. The field geometry of MWDs can be derived, however, from the analysis of the pure Zeeman splitting of the photospheric lines and their circular polarization properties as a function of rotational phase. Because of the large Zeeman shifts, this approach must include the whole optical range for $B \gtrsim 50$ MG. In the absence of positional information from the Doppler effect, however, the inversion of the flux and polarization spectra is an intricate task. Trial-and-error fits of centred or shifted dipoles and quadrupoles (Wickramasinghe & Cropper 1988; Putney & Jordan 1995) are incapable of exploring the full parameter space of possible solutions. We present a new strategy using a pre-computed database of synthetic MWD spectra and an automatic quality-of-fit optimization algorithm.

A first approach along these lines was presented by Donati et al. (1994), who used a maximum entropy algorithm (MEM) to fit a matrix of areal filling factors for a grid of synthetic flux and circular polarization spectra to simulated input data. This way, they obtained the "simplest" and, according to *Occam's razor*, most likely frequency distribution of transverse and longitudinal field strengths over the visible stellar disc at each rotational phase, a so-called ZEBRA plot, but this approach does not provide any information about the spatial structure of the magnetic field.

In this paper, we investigate to what extent the underlying global magnetic field distribution can be recovered directly from least-squares fits to phase-resolved flux and polarization

Send offprint requests to: F. Euchner,
e-mail: feuchner@uni-sw.gwdg.de

spectra of a given signal-to-noise ratio. This approach uses the spatial information provided by the magnetic fields seen at different rotational phases and has the advantage that the uncertainties in the parameters describing the global field structure can be directly related to the noise in the spectra. Its disadvantage lies in the necessary restriction to model fields which can be described by a sufficiently small number of parameters.

We assume fields which can be represented by centred or offset dipole and quadrupole components which need not be aligned with each other. The specific geometries tested here include a star with a single high-field spot and one with two spots separated by $\sim 90°$. Our computer code allows us to calculate areal filling factor matrices analogous to ZEBRA plots, the resulting flux spectra, and the wavelength-dependent circular polarization for a given magnetic field model viewed at a number of rotational phases. We compare the results with the reference input (which are simulated data in this case) and determine the best-fit parameters using an evolutionary optimization strategy.

The present paper is arranged as follows. In Sect. 2 we describe the database of flux and polarization spectra computed for a wide range of field strengths, viewing angles, and effective temperatures. Section 3 describes the general design of the magnetic field models and Sect. 4 the construction of the integrated spectra from the database for a given model of the magnetic field. Section 5 explains the optimization code, describes the specific field models subjected to the reconstruction tests, and investigates the ability of the code to deduce the respective field parameters from the integrated flux and polarization spectra. Finally, the power and also the limitations of our approach are discussed in Sect. 6.

In forthcoming papers, we will analyse phase-resolved spectral flux and circular polarization data of MWDs obtained at the ESO VLT.

2. The database

2.1. Radiative transfer for Magnetic White Dwarfs

Our synthetic Zeeman spectra and wavelength-dependent polarization data are computed with the most recent version of the code developed by S. Jordan. The polarization originates from the different absorption coefficients κ_l, κ_r, and κ_p for left- and right-handed circularly polarized light, and linearly polarized light travelling perpendicularly to the magnetic field, respectively, and is described by the four Stokes parameters I, Q, V, and U. The influence of the Faraday rotation and the Voigt effect is accounted for by the magneto-optical parameters ρ_R and ρ_W. The three radiative transport equations of Unno (1956) then expand into four equations (Beckers 1969; Hardorp et al. 1976) which can be solved by one of several different algorithms: (a) the method of Wickramasinghe & Martin (1979) assumes that the source function is linear in the optical depth and that between two successive depth points the Stokes parameters can be described by exponential functions; (b) direct Runge-Kutta integration; (c) accelerated Λ iterations (Takeda 1991); (d) an approximation for large Faraday rotation (Ramaty 1969); or (e) matrix exponential solutions (Dittmann 1995). Intensive tests performed by H. Schmidt and S. Jordan in Kiel have demonstrated the numerical equivalence of these methods with high accuracy. For the present paper, we have calculated an extensive database of synthetic flux and circular polarization spectra using Ramaty's approximation, which is always justified in white dwarf atmospheres, and is rather efficient with regard to CPU time.

The temperature and pressure structure of our atmospheres is taken from zero field LTE models (Koester et al. 1979). As a consequence, the magnetic pressure and magnetic blanketing (Jordan 1992) have been neglected. Convection is assumed to be suppressed by the field (Jordan 2001). For the line opacities, data from the Tübingen group (Forster et al. 1984; Rösner et al. 1984; Wunner et al. 1985) were used. Bound-free opacities were calculated using a modified approximation by Lamb & Sutherland (1974) which leads to small errors only (Jordan 1992; Merani et al. 1995; Jordan & Merani 1995) and saves an enormous amount of computing time. The approach described here was developed in two diploma theses (Euchner 1998; Rahn 1999) and was also implemented by Burleigh et al. (1999).

2.2. Database spectra

We computed a three-dimensional grid of Stokes I and V model spectra with the effective atmospheric temperature T, the magnetic field strength B, and the field direction ψ relative to the line of sight as the independent variables. We considered T = 8000 K, 9000 K, 10 000 K, 11 000 K, 12 000 K, 13 000 K, 15 000 K, 17 000 K, 20 000 K, 25 000 K, 30 000 K, 40 000 K, B = 10 MG to 200 MG in steps of 1 MG, and $\psi = 0°$, 29°, 41°, 51°, 60°, 68°, 76°, 82°, 90°, i.e., equidistant in $\cos\psi$. This yields a database containing $12 \times 191 \times 9 = 20\,628$ model spectra for I and V each. All spectra are calculated for a surface gravity of $\log g = 8$. Since we do not include the linear polarization, the field direction is sufficiently constrained by the total field strength and the longitudinal field component. As an example, Fig. 1 shows a section around Hα for a sample of database spectra with T = 15 000 K, B = 20 MG and five angles of ψ, equally spaced in $\cos\psi$. A typical property of these Zeeman spectra is the weak angular dependence of Stokes I, except near 0° and 90°, and the more pronounced dependence of Stokes V. Somewhat simplified, Stokes I carries much of the information on the distribution of the absolute value of $\boldsymbol{B}$ over the surface of the star, while Stokes V is needed to derive the distribution of the field directions.

If limb darkening is important the direction cosine μ of the line of sight with respect to the vertical direction in the stellar atmosphere needs to be considered as a further parameter in the database. Hence, including a wavelength-dependent description of limb darkening requires an expansion of the number of model spectra in the database by a factor equal to the number of μ-values considered. For the present calculations, we use a simple limb darkening law which is independent of wavelength and avoid this extension of the database (see Sect. 4.3 below).

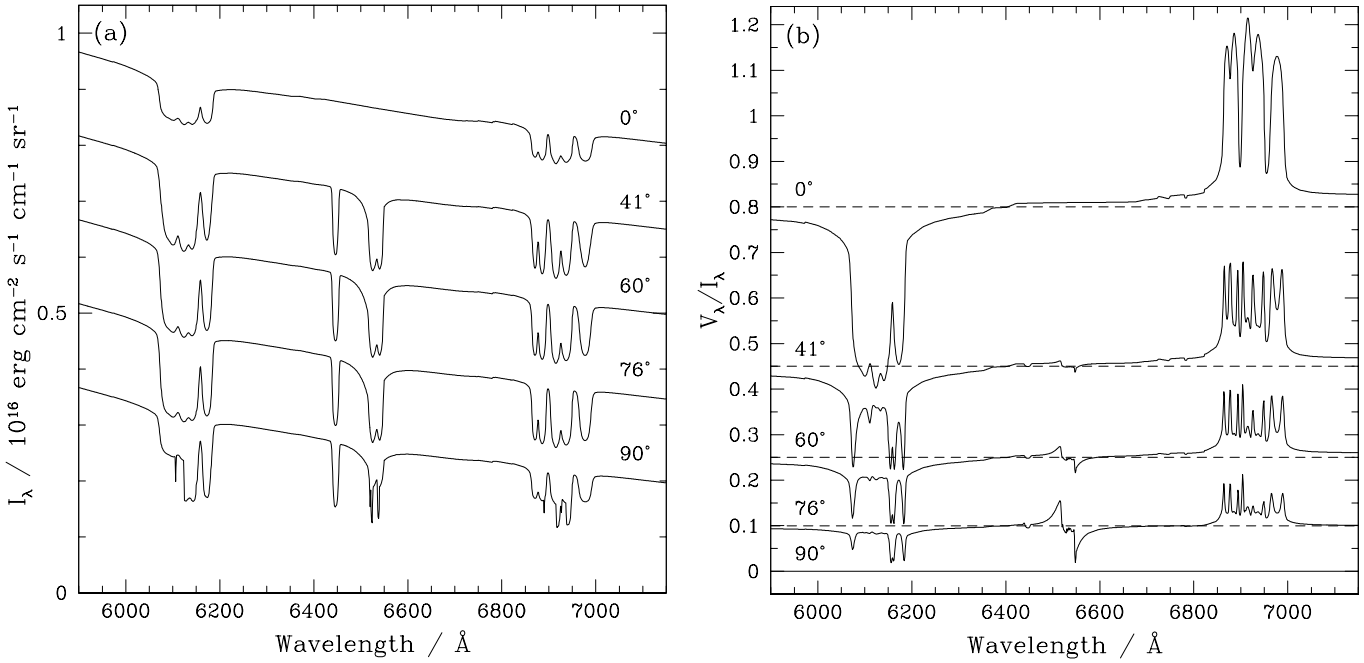

Fig. 1. Examples of the database spectra for $B = 20$ MG, $T = 15\,000$ K, and five angles of ψ equally spaced in $\cos\psi$ covering the Hα σ^--, π-, and σ^+-components. **a)** Intensity, **b)** degree of circular polarization. The spectra are shifted vertically by arbitrary amounts to avoid overlap.

3. Magnetic field geometry

A curl-free field which originates only from sources in the stellar interior can be described by a multipole expansion of the scalar magnetic potential, using spherical harmonics with coefficients l and $m = 0, \ldots, l$, which describe the zonal and sectoral periodicity of the field, respectively (see, e.g., Langel 1987). The number of free parameters of the field geometry is $l(l+2)$, i.e. 8 (15) for $l = 2$ (3). Defining the viewing geometry requires three additional parameters for the orientation of the rotation axis and the inclination.

The optimization procedure adopted for the present tests can handle only a limited number of multipole parameters and becomes inefficient already when the octupoles ($l = 3$) are included. We have restricted the complexity of the field, therefore, by including only the two lowest zonal harmonics, commonly referred to as "dipole" ($l = 1$, $m = 0$) and "quadrupole" ($l = 2$, $m = 0$), allowing their axes to be inclined with respect to each other. We do not consider the $m = 1$ and $m = 2$ quadrupoles, but instead include a common offset of the dipole-quadrupole combination from the centre of the star. This hybrid model has ten free parameters: two polar field strengths; two angles each for the directions of the axes relative to the rotation axis; the three components of the offset; and the inclination, i.e. the angle between the rotation axis and the line of sight. An offset from the centre was included because of its popularity and simplicity (e.g., the Earth's magnetic field is approximately that of a shifted dipole). The chosen field structure deliberately includes some very similar field geometries described by different sets of parameters: a combination of aligned dipole and quadrupole can be approximated by a shift of the dipole. At sufficient signal to noise, the reconstruction procedure can distinguish between such geometries, a result which is of interest by itself. While our hybrid model is useful for the tests performed in this paper, its limited complexity may not suffice for the interpretation of real, observed spectra.

We consider rotating MWDs viewed at an inclination i with respect to the rotation axis. Note that a fraction $f = 0.5\,(1 - \sin i)$ of the stellar surface is permanently hidden from view and that phase-resolved Zeeman spectroscopy provides no information on the field on this hidden fraction of the surface. In order to save computing time, we restrict ourselves to simultaneously fitting flux and polarization spectra at four rotational phases, $\phi = 0.0$, 0.25, 0.5, and 0.75. We avoid a special geometry by choosing $\phi = 0$ not to coincide with the nearest approach of one of the axes to the line of sight.

Since observational restrictions often prevent taking phase-resolved data, we also consider the amount of information which can be retrieved from a single flux and polarization spectrum or even a single flux spectrum only. In this case, the data provide information on the magnetic field structure only for one hemisphere of the star.

At any given phase ϕ, the polarization depends on the components of the field transverse and parallel to the line of sight. In order to describe these components, we introduce four Cartesian coordinate systems (Figs. 2a and 2b): (i, ii) systems Σ' and Σ'', in which z' and z'' describe the dipolar and quadrupolar axes of symmetry, respectively; (iii) the observer's system Σ, in which the x-axis points towards the observer and the z-axis lies in the plane defined by the x-axis and the rotation axis; and (iv) the auxiliary system Σ_0 with z_0 the direction of the rotation axis which defines the inclination angle i. The rotational phase angle $\omega = 2\pi\phi$ is defined with respect to the direction of the x_0-axis which lies in the x-z-plane for $\omega = 0$.

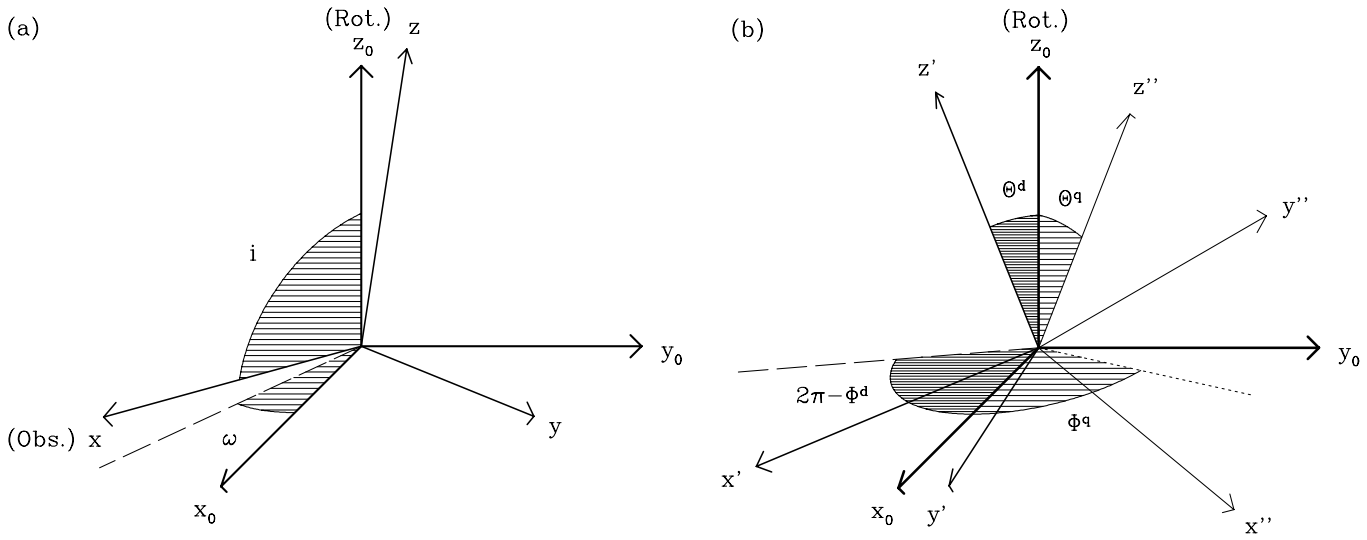

Fig. 2. a) Rotational geometry of the MWD models. The x-axis points towards the observer, the z_0-axis marks the rotation axis. The dashed line marks the intersection of the x-z-plane with the x_0-y_0-plane. i denotes the inclination, and ω the rotational phase angle. **b)** Magnetic geometry of the MWD models. The z'- and z''-axes mark the axes of symmetry for the dipole and quadrupole components. The lines of intersection of the x'-z'-plane and the x''-z''-plane with the x_0-y_0-plane are given by the dashed and the dotted lines, respectively.

The components of the surface field $\boldsymbol{B}(\boldsymbol{r}')$ of the centred dipole in system Σ' are

$$(B^{\rm d})_{x'} = 3B^{\rm d}_{\rm pol}\, x'z'/(2r'^5), \quad (1)$$

$$(B^{\rm d})_{y'} = 3B^{\rm d}_{\rm pol}\, y'z'/(2r'^5), \quad (2)$$

$$(B^{\rm d})_{z'} = B^{\rm d}_{\rm pol}(3z'^2 - r'^2)/(2r'^5), \quad (3)$$

with $\boldsymbol{r}' = (x', y', z')$ and $|\boldsymbol{r}'|^2 = r'^2 = x'^2 + y'^2 + z'^2$. Correspondingly, the components of the centred quadrupole in Σ'' are

$$(B^{\rm q})_{x''} = B^{\rm q}_{\rm pol}\, x''(5z''^2 - r''^2)/(2r''^7), \quad (4)$$

$$(B^{\rm q})_{y''} = B^{\rm q}_{\rm pol}\, y''(5z''^2 - r''^2)/(2r''^7), \quad (5)$$

$$(B^{\rm q})_{z''} = B^{\rm q}_{\rm pol}\, z''(5z''^2 - 3r''^2)/(2r''^7), \quad (6)$$

with $\boldsymbol{r}'' = (x'', y'', z'')$ and $|\boldsymbol{r}''|^2 = r''^2 = x''^2 + y''^2 + z''^2$. Σ' and Σ'' are tilted with respect to the rotation axis z_0 by angles $\Theta^{\rm d}$ and $\Theta^{\rm q}$, respectively. The azimuth angles of the tilt in Σ_0 are $\Phi^{\rm d}$ and $\Phi^{\rm q}$ at phase $\phi = 0$. We apply the appropriate rotations and the translation to transform the fields into the observer's system Σ, add the dipole and quadrupole components, and obtain $\boldsymbol{B}(\boldsymbol{r})$ for each surface element, with $B_x = B_{\rm l} = B\cos\psi$ the longitudinal component of the field.

The angle δ between the dipole and quadrupole axes and the angles $\eta^{\rm d}$ and $\eta^{\rm q}$ between the line of sight at phase ϕ and the dipole and quadrupole axis, respectively, are given by

$$\cos\delta = \cos\Theta^{\rm d}\cos\Theta^{\rm q} + \sin\Theta^{\rm d}\sin\Theta^{\rm q}\cos(\Phi^{\rm q} - \Phi^{\rm d}), \quad (7)$$

$$\cos\eta^{\rm d} = \cos i\,\cos\Theta^{\rm d} + \sin i\,\sin\Theta^{\rm d}\cos(2\pi\phi + \Phi^{\rm d}), \quad (8)$$

$$\cos\eta^{\rm q} = \cos i\,\cos\Theta^{\rm q} + \sin i\,\sin\Theta^{\rm q}\cos(2\pi\phi + \Phi^{\rm q}). \quad (9)$$

Our magnetic geometries were selected for the purpose of providing sufficient complexity for an effective test of our reconstruction routine. The offset $\boldsymbol{r}'_{\rm off}$ from the centre is a simple means of producing a substantial amount of azimuthal asymmetry if $\boldsymbol{r}'_{\rm off}$ is perpendicular to the dipole axis, while $\boldsymbol{r}'_{\rm off}$ parallel to the dipole axis allows to test the ability of the routine to distinguish between aligned centred dipole-quadrupole combinations and a shifted dipole.

4. Input spectra for the reconstruction procedure

4.1. Integration of the database models

We divide the spherical star into surface elements defined by equal steps in latitude and longitude. For given distributions of the magnetic field vector $\boldsymbol{B}$ and the effective temperature T over the surface, let α be the running index of the surface elements which are visible at a given rotational phase $0 \geq \phi \geq 1$ and which have sizes A_α, central field strengths B_α, field directions ψ_α, and direction cosines μ_α. The Stokes parameters $\langle I_\lambda\rangle$ and $\langle V_\lambda\rangle$ are then computed as weighted sums of the individual contributions corrected for limb darkening by a factor $f^{\rm LD}_\alpha$ (discussed below)

$$\begin{pmatrix}\langle I_\lambda\rangle\\ \langle V_\lambda\rangle\end{pmatrix}(\phi) = \sum_{\alpha(\phi)} A_\alpha\mu_\alpha f^{\rm LD}_\alpha \begin{pmatrix} I_{\lambda,\alpha}\\ V_{\lambda,\alpha}\end{pmatrix}. \quad (10)$$

We represent the wavelength-dependent contributions $I_{\lambda,\alpha}$ and $V_{\lambda,\alpha}$ from surface element α by appropriate interpolation in the database grids of the parameters T, B, and ψ. For T and ψ, a bilinear interpolation suffices. For the field strength, we consider all spectra representative of the B-variation over the finite surface element. We found that a number of 900 surface elements per hemisphere is a good compromise between CPU time and needed accuracy. This number is sufficient to avoid spectral structure caused by the finite element size.

Our code can account for temperature variations over the surface of the white dwarf, but in this paper we consider only stars with uniform surface temperatures.

4.2. Relation to the observed flux

The flux observed from a star of radius R at distance d is

$$f_\lambda = F_\lambda R^2/d^2 \tag{11}$$

where $F_\lambda = \pi \langle I_\lambda \rangle$ is a function of T, for a given magnetic field distribution. The interpretation of observed Zeeman spectra in terms of $\langle I_\lambda \rangle$ and $\langle V_\lambda \rangle$ involves T and R/d as fit parameters.

For the present tests, T and R/d are considered as fixed parameters and the quantities fitted by variation of the field parameters are F_λ and $V/I = \langle V_\lambda \rangle / \langle I_\lambda \rangle$ ·

4.3. Limb darkening

We have compared (i) the full radiative transfer for each surface element which accounts for the μ-dependence and the variation of B across the element already in the atomic data, (ii) an interpolation between the spectra for discretized μ and B, and (iii) the application of a wavelength-independent linear limb darkening law replacing the interpolation in μ. Method (ii) uses spectra calculated for $\mu = 0.1$, 0.4, 0.7, and 1.0. Method (iii) employs a linear law with coefficients which are valid for the visible wavelength range,

$$f_\alpha^{\rm LD} = I_\lambda(\mu)/I_{\lambda,\mu=1} = 0.70 + 0.30\mu. \tag{12}$$

Test calculations for the three approaches (i) to (iii) were performed for centred dipoles viewed pole-on with polar field strengths of (A) 200 MG, (B) 80 MG, and (C) 30 MG. We found the differences between (i) and (ii) to be minute. Case (iii) differs by a wavelength-dependent factor which arises from the neglect of any wavelength dependence in the limb darkening approximation. Figure 3 shows the results for cases (ii) and (iii) at an effective temperature of 15 000 K. For all three field strengths, the spectra computed for case (iii) deviate by at most 5% from those of cases (i) and (ii). The insert shows that the absorption lines are about 2% deeper than for the correct treatment.

The simple limb darkening law of Eq. (12) is entirely acceptable for the present tests which interpret synthetic spectra with spectra of the same origin. The above comparison suggests, moreover, that a wavelength-independent linear limb darkening law may also be acceptable for the interpretation of observed optical Zeeman spectra of white dwarfs.

5. Reconstruction of the field geometry

In this section, we describe a variety of magnetic field and viewing geometries and test the ability of our code to reconstruct their parameters from flux and circular polarization spectra at $\phi = 0.0$, 0.25, 0.5, and 0.75. All calculations were performed for an effective temperature of 15 000 K. In order to simulate real data, noise was added to the input spectra at the four phases as described below. Because of the added noise, the reconstructed field is not necessarily identical to the input field. For the present tests, the wavelength range was restricted to $4000 \le \lambda \le 7600$ Å, which contains the most important Balmer line components, and all spectra were rebinned into 10 Å bins, yielding 361 data pixels per spectrum, a total of 1444 pixels in the combined flux spectra at four rotational phases, and another 1444 pixels in the polarization spectra.

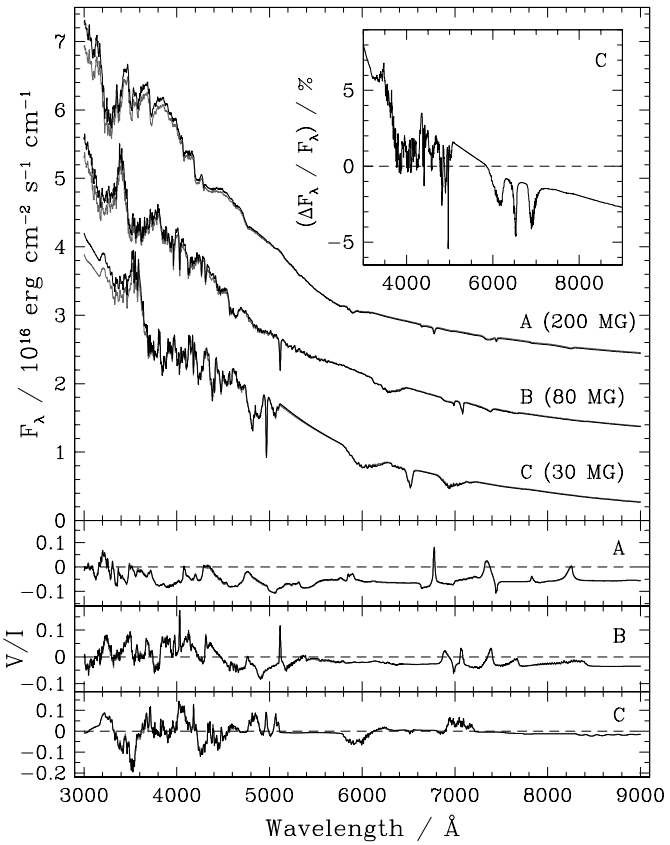

Fig. 3. Spectral flux *(top)* and circular polarization *(bottom)* for centred dipoles viewed pole-on with polar field strengths of (A) 200 MG, (B) 80 MG, and (C) 30 MG for $T = 15\,000$ K. The library-based spectra computed using a database of four μ-values (grey) are compared to those for $\mu = 1$, corrected with a mean limb darkening law (black). Spectra (A) and (B) have been shifted upwards to avoid overlap (1.1 flux units each). The insert shows the relative flux differences for the 30 MG case (C).

5.1. Magnetic field models

We define seven different magnetic field and viewing geometries against which we test our reconstruction code. The field configurations (A) to (F) are characterized by an increasing level of complexity. The geometrical and spectral properties of the models are summarized in Figs. 4–7. In each case, the centre panel shows the distributions of the total field strength B and of the absolute value of the longitudinal component B_l over the visible hemisphere at the four selected phases. The + and − symbols indicate the sign of the longitudinal component. The range of field strengths realized over the visible part of the surface of the white dwarf is given by the top grey bar. The left-hand panel shows the B–ψ diagram, a greyscale plot of the frequency distribution of the magnetic field strength B and the direction cosine $\cos\psi$. The fractional contribution of each single database spectrum to the integrated spectrum is represented by the greyscale value of the corresponding pixel in the plot. This presentation includes the effects of pixel area, foreshortening,

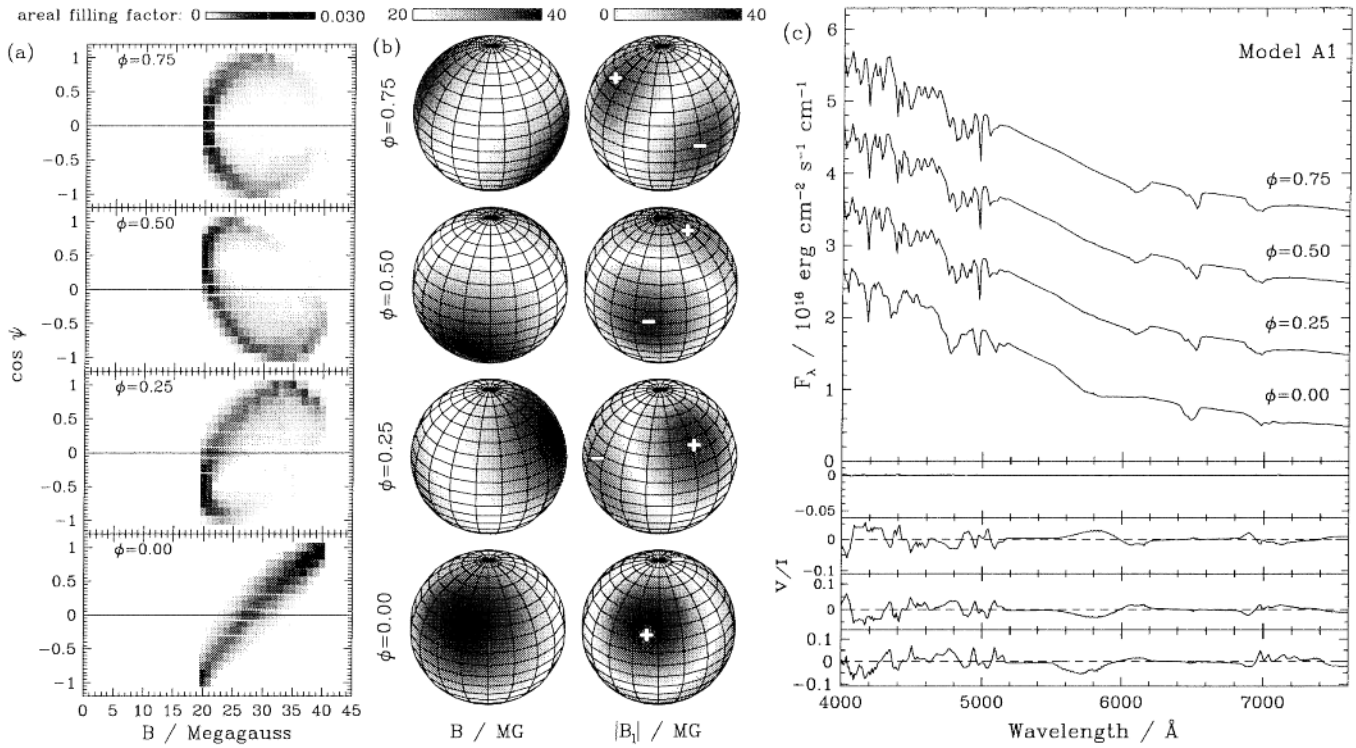

Fig. 4. Model (A1), centred dipole viewed at $i = 60°$: **a)** B–ψ diagram, **b)** field strength and longitudinal component, **c)** flux and polarization spectra. The + and − symbols indicate the sign of the longitudinal component of the magnetic field. For clarity, the flux spectra at $\phi = 0.25$, 0.5, and 0.75 have been shifted upwards by one flux unit each.

and limb darkening. The sum of all filling factors would be unity if limb darkening were neglected, but falls below unity with limb darkening included. The B–ψ diagrams are equivalent to the ZEBRA plots of Donati et al. (1994), except for the effect of limb darkening which was not included by these authors. The diagrams illustrate the change in the weighting of the two main database parameters, B and ψ, as the star rotates. The right-hand panel shows the resulting integrated flux and circular polarization spectra at the four rotational phases.

Model (A1), centred dipole viewed at $i = 60°$: the polar field strength is $B^{\rm d}_{\rm pol} = 40$ MG and the axis points towards ($\Theta^{\rm d}$, $\Phi^{\rm d}$) = (60°, 340°). This oblique rotator model stands for a simple low-field geometry. The hidden fraction is only 7% of the white dwarf surface. The flux spectra in Fig. 4c are quite similar at $\phi = 0.25, 0.5$, and 0.75, but the circular polarization spectra are not. The B–ψ diagram looks different at $\phi = 0$ and so does the flux spectrum. These differences suggest that full phase coverage is essential for a successful recovery of the field geometry.

Model (A2), centred dipole viewed at $i = 30°$: the hidden fraction of the surface is now 25%. Otherwise, the properties of the model (Fig. 5, top) are similar to (A1). For the centred dipoles of models (A1) and (A2), the circular polarization vanishes at a phase ϕ_0, where the dipole axis is oriented perpendicular to the line of sight.

Model (B), centred quadrupole viewed at $i = 60°$: the polar field strength is $B^{\rm q}_{\rm pol} = 40$ MG and the axis points towards ($\Theta^{\rm q}$, $\Phi^{\rm q}$) = (60°, 340°). Figure 5c (bottom) shows that there is little rotational variation. The flux spectra and the polarization vary little for $\phi = 0.25, 0.5$, and 0.75, but differ at $\phi = 0$.

Model (C), aligned centred dipole and quadrupole viewed at $i = 60°$: a quadrupole of $B^{\rm q}_{\rm pol} = 20$ MG is added to a dipole of $B^{\rm d}_{\rm pol} = 40$ MG with ($\Theta^{\rm d}$, $\Phi^{\rm d}$) = ($\Theta^{\rm q}$, $\Phi^{\rm q}$) = (60°, 340°). The asymmetry introduced into the field geometry causes larger rotational variations in flux and polarization than for the pure dipole or quadrupole (Fig. 6c, top).

Model (D), shifted high-field dipole viewed at $i = 60°$: the polar field strength is $B^{\rm d}_{\rm pol}$= 110 MG, offset in all three coordinates by ($x'_{\rm off}$, $y'_{\rm off}$, $z'_{\rm off}$) = (0.05, −0.10, 0.15). The shift along the dipole axis increases the maximum field, and the sideways shift decreases the minimum field to the effect that B ranges from 39 to 192 MG. That is, B varies by a factor of five compared to a factor of two for the centred dipole. The high field causes the flux spectra to show substantially less structure than in the previous models, suggesting that a higher signal-to-noise ratio is needed for reconstruction (Fig. 6c, bottom). There is substantial variation in the circular polarization over the rotational period, however, which helps in the reconstruction.

Model (E), shifted dipole viewed at $i = 60°$: this is an extremely off-centred dipole with $B^{\rm d}_{\rm pol} = 58$ MG and ($x'_{\rm off}$, $y'_{\rm off}$, $z'_{\rm off}$) = (0.15, −0.10, 0.30) which displays a variation of B over the surface by nearly a factor of 12. For one half of the rotational period, the high-field pole is in view, over the other half the field distribution is concentrated at low field strengths. Effectively, this represents a star with a low field of around 20 MG over most of the star and a spot in which the field rises

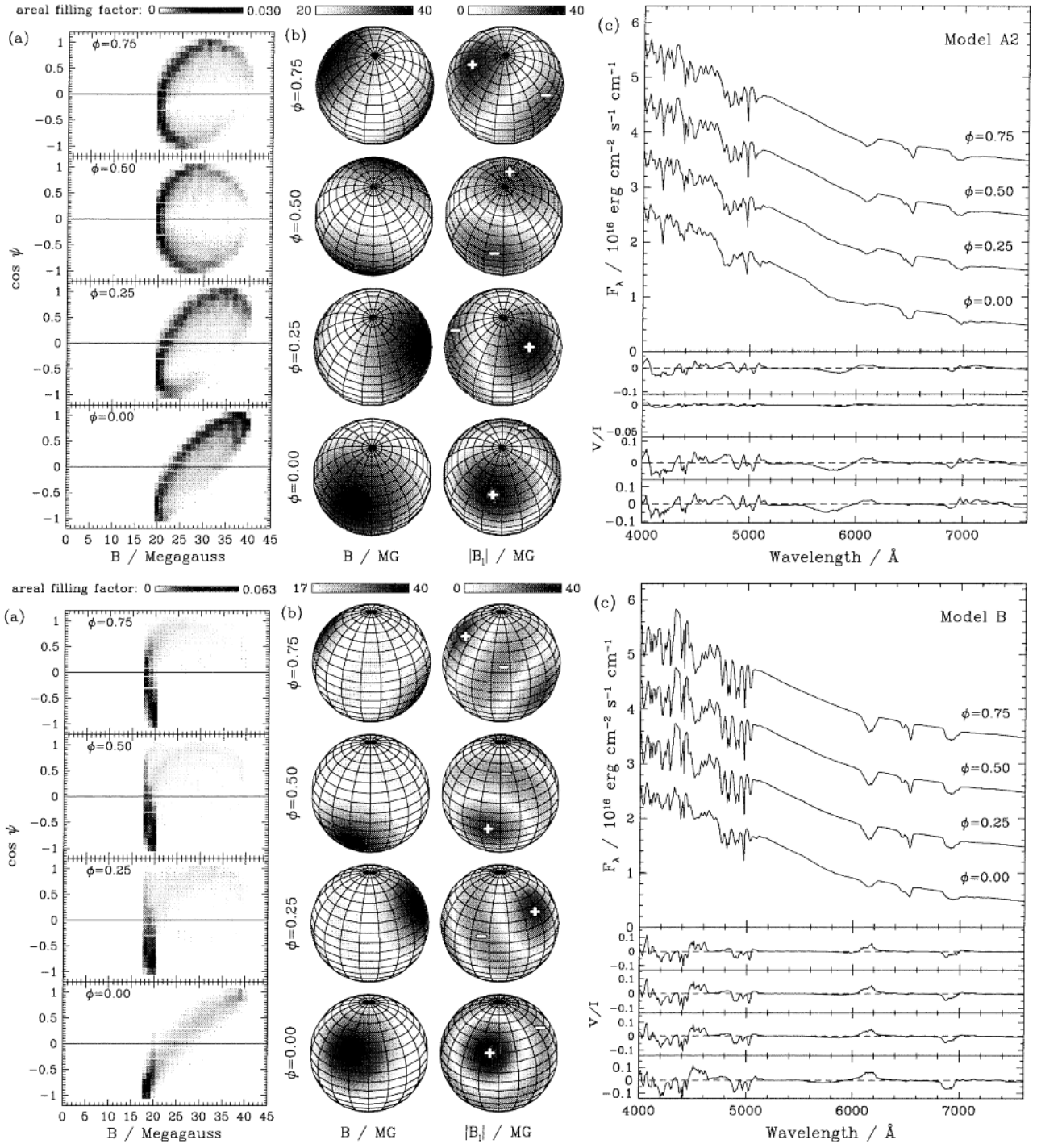

Fig. 5. *Top:* model (A2), centred dipole viewed at $i = 30°$: **a)** B–ψ diagram, **b)** field strength and longitudinal component, **c)** flux and polarization spectra. *Bottom:* model (B), pure quadrupole viewed at $i = 60°$: **a)** B–ψ diagram, **b)** field strength and longitudinal component, **c)** flux and polarization spectra. See Fig. 4 for further explanation.

to 198 MG. The circular polarization displays pronounced rotational structure (Fig. 7c, top).

Model (F), non-aligned dipole-quadrupole combination viewed at $i = 60°$: this is the most complex field model featuring the superposition of a non-aligned dipole and quadrupole with equal polar field strengths of 40 MG. The polar directions, $(\Theta^d, \Phi^d) = (60°, 340°)$ and $(\Theta^q, \Phi^q) = (30°, 250°)$, are separated by 64°. The field geometry features two high-field spots, an upper positive and a lower negative one, which are dominated by the quadrupole and the dipole, respectively, and are separated by ∼90° (Fig. 7, bottom).

An overview of the models (A)–(F) is given in Table 1. To illustrate the effects of noise in the spectra used in the reconstructions, we show in Fig. 8 the flux and polarization spectra of Model (A1) for $\phi = 0$ at noise levels of $S/N = 100$ and $S/N = 20$.

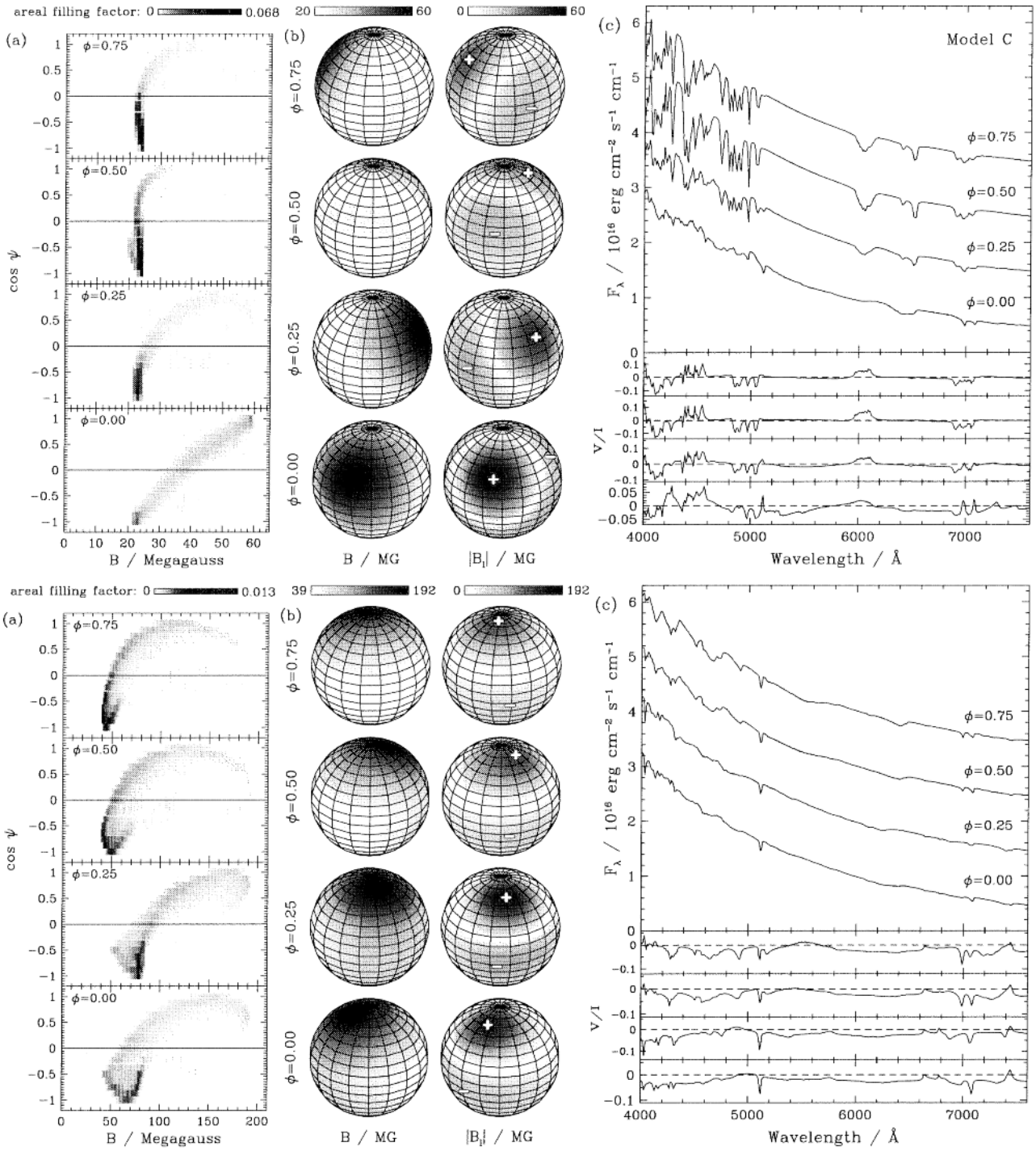

Fig. 6. *Top:* model (C), aligned dipole and quadrupole viewed at $i = 60°$: **a)** B–ψ diagram, **b)** field strength and longitudinal component, **c)** flux and polarization spectra. *Bottom:* model (D), shifted high-field dipole viewed at $i = 60°$: **a)** B–ψ diagram, **b)** field strength and longitudinal component, **c)** flux and polarization spectra. See Fig. 4 for further explanation.

5.2. Optimization algorithm

Our spectral synthesis method is sufficiently fast to allow the use of hierarchical search strategies in the parameter space. We utilize the optimization routine evoC (Trint & Utecht 1994) that implements an evolutionary strategy algorithm (Rechenberg 1994), and has proven useful already in other astrophysical contexts (Gänsicke & Beuermann 1996; Gänsicke et al. 1998; Kube et al. 2000). The task is to find a set $\boldsymbol{a} = (a_1, \ldots, a_M)$ of M free parameters that minimizes the classic penalty function

$$\chi^2_{\rm red}(\boldsymbol{a}) = \frac{1}{N-M} \sum_{j=1}^{N} \frac{(f_j - s_j(\boldsymbol{a}))^2}{{\sigma_j}^2} \tag{13}$$

given the input data pixels f_j, the model data pixels s_j, and the standard deviations σ_j. Good fits require $\chi^2_{\rm red} \approx 1$. We have

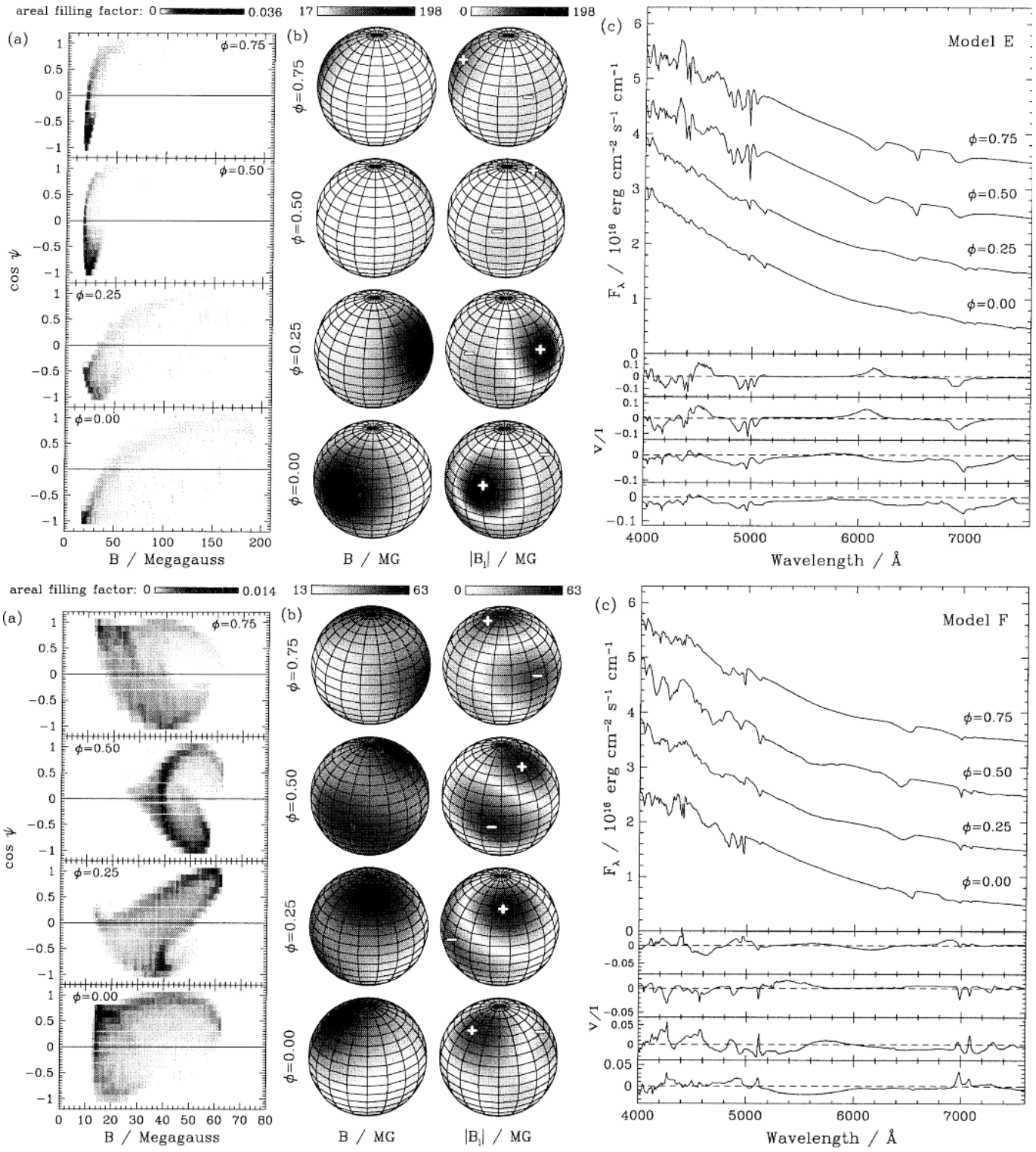

Fig. 7. *Top:* model (E), shifted dipole viewed at $i = 60°$: **a)** B–ψ diagram, **b)** field strength and longitudinal component, **c)** flux and polarization spectra. *Bottom:* model (F), non-aligned dipole-quadrupole combination viewed at $i = 60°$: **a)** B–ψ diagram, **b)** field strength and longitudinal component, **c)** flux and polarization spectra. See Fig. 4 for further explanation.

applied Gaussian noise to the input spectra to yield signal-to-noise ratios, corresponding to relative standard deviations in F_λ and absolute standard deviations in V/I, of 0.01 and 0.05, respectively. For fits to fluxes only, j runs up to $N = 1444$, and, for fits to both flux and polarization, up to $N = 2888$.

For each field model and each reconstruction with a certain set of free parameters, the `evoC` optimization process is run repeatedly, typically 6–20 times, starting each run with different, randomly chosen parameter values. Not all runs end up in the global minimum. A misguided run may be caught in a

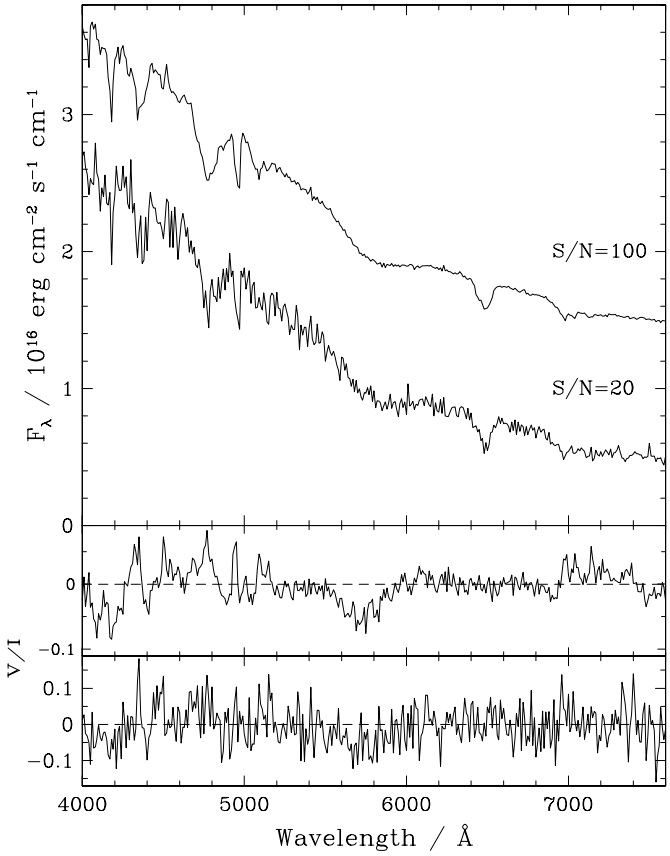

Fig. 8. Examples of simulated spectra used as input to the reconstruction procedure. The $\phi = 0$ spectrum of Model (A1) is shown with a signal-to-noise ratio $S/N = 20$ and 100 (shifted upwards by one flux unit). *Top:* flux spectra, *bottom:* circular polarization spectra.

local minimum corresponding to an incorrect field configuration, which nevertheless has a Zeeman spectrum similar to the input one. We define a success rate of the optimization as the fractional number of runs which reach a best-fit $\chi^2_{\rm red} < 2.0$ for $S/N = 100$, and $\chi^2_{\rm red} < 1.1$ for $S/N = 20$ (corresponding virtually always to the global minimum). As a last finish, we employ a downhill simplex algorithm (Nelder & Mead 1965; Press et al. 1992) on the run with the best $\chi^2_{\rm red}$, which sometimes improves on the `evoC` solution.

In order to illustrate the problem associated with local minima in the χ^2-landscape, we present in Fig. 9 a simple example of different field geometries which yield similar Zeeman spectra. The input geometry is the sum of a (non-rotating) dipole with $B^{\rm d}_{\rm pol} = 40\,{\rm MG}$ and an aligned quadrupole with $B^{\rm q}_{\rm pol} = 20\,{\rm MG}$, viewed at $i = 60°$ (with $\Theta^{\rm d} = \Theta^{\rm q} = \omega = 0°$, Fig. 2). The right-hand panel of Fig. 9 shows the corresponding flux and polarization spectra (lower curves). We add Gaussian noise of $S/N = 100$ and compute flux and flux+polarization spectra covering a range of quadrupole parameters, with the dipole parameters and the inclination kept fixed. The quadrupole is allowed to vary in strength and orientation with $\Theta^{\rm q}$ free at $\Phi^{\rm q} = 90°$. For this choice of parameters, the quadrupole is perpendicular to the dipole and to the line of sight for $\Theta^{\rm q} = 90°$. The left-hand panel of Fig. 9 shows a contour plot of the χ^2-landscape for the spectral flux in the $B^{\rm q}_{\rm pol}$,$\Theta^{\rm q}$-plane. Besides the global minimum at the parameter values of the input configuration ($B^{\rm q}_{\rm pol} = 20\,{\rm MG}$, $\Theta^{\rm q} = 0°$), a second pronounced minimum appears at $B^{\rm q}_{\rm pol} = -17\,{\rm MG}$ and $\Theta^{\rm q} = 90°$, with the minus sign indicating a reversed polarity of the quadrupole. The flux and circular polarization spectra for this minimum are also shown in the right-hand panel of Fig. 9. At moderate noise levels, the flux and polarization spectra of these two diverse field geometries become indistinguishable and it is not surprising that the local minimum (in the upper left corner of the contour plot) persists if flux and circular polarization are considered together. The shallow local minimum at $B^{\rm q}_{\rm pol} \simeq 33\,{\rm MG}$, $\Theta^{\rm q} \simeq 80°$, on the other hand, disappears if V/I is included in the computation of $\chi^2_{\rm red}$. In the centre panels of Fig. 9, the B–ψ diagrams for both configurations are shown. Both distributions are sufficiently similar if projected either on the B-axis or on the $\cos\psi$-axis to explain why the spectra are similar, but not identical.

Finally, we note that fitting the remaining parameters of the field model (like $B^{\rm d}_{\rm pol}$) instead of keeping them fixed would cause the local minima to become even more pronounced. Increased noise also deepens the local minima relative to the global one. A local χ^2-minimum is responsible for an incorrect, although not entirely dissimilar, reconstruction of Model F discussed below.

5.3. Reconstruction fits

5.3.1. General characteristics of the solutions

Depending on the complexity of the input field, we consider reconstructions which differ in the numbers of free parameters, ranging from the full set of ten down to seven (with the quadrupole component or the offset neglected). Some redundancy is allowed because a dipole offset along its axis can also be modelled, to first order, by an aligned centred dipole-quadrupole combination. With data of sufficient S/N, the reconstruction procedure can recognize such subtle differences.

As a general feature, the reconstructed global field is of relevance only for that part of the stellar surface which is visible during the observation (or covered by the synthetic input in this paper). This underlines the importance of phase-resolved observations which allow the determination of the inclination and, thereby, to estimate the occulted fraction of the surface.

Spectrophotometry of high S/N is obtained more easily than spectropolarimetry of the same quality. The observer has to decide, therefore, whether a given amount of observing time is better spent on high-quality spectrophotometry or on circular spectropolarimetry of lower quality. In order to address such questions, we reconstructed all field geometries, using the spectral flux *and* the polarization, and using the spectral flux only. The flux-only reconstructions are successful in several cases, but the deviations from the input geometry tend to be larger, and an increased number of non-convergent runs suggest a less well-behaved χ^2-landscape. We find that the circular polarization is not needed in simple cases, while its inclusion is extremely useful for the reconstruction of more complex fields.

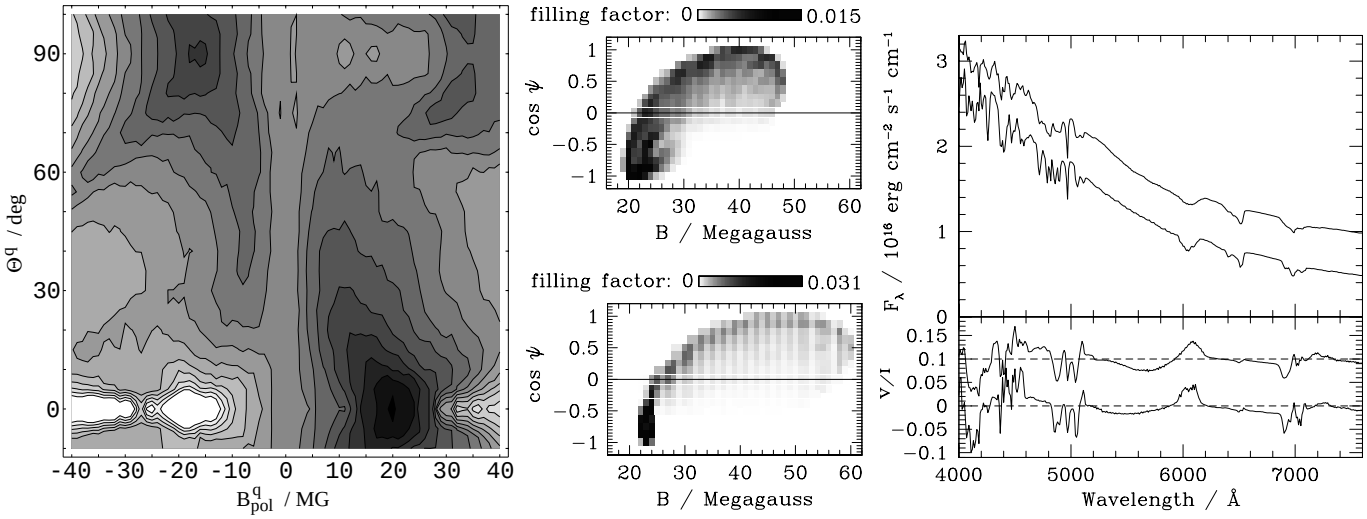

Fig. 9. *Left panel:* contour plot of the χ^2-landscape for the spectral flux in the $B^{\rm q}_{\rm pol}$,$\Theta^{\rm q}$-plane. The input configuration is given by $B^{\rm d}_{\rm pol} = 40$ MG, $B^{\rm q}_{\rm pol} = 20$ MG, and $\Theta^{\rm d} = \Theta^{\rm q} = 0°$. Darker shading corresponds to smaller values of $\chi^2_{\rm red}$. *Centre panel: B–ψ* diagrams of the field configurations corresponding to the local *(top)* and the global *(bottom)* minimum. *Right panel:* flux and circular polarization spectra corresponding to the the global minimum (lower curves) and the local minimum in the upper left of the left panel (upper curves, shifted upwards by 0.5 units in flux and 0.1 units in polarization).

5.3.2. Results for individual field geometries

In this section, we present the results for the reconstructions of the input models (A) to (F), using the spectra at four rotational phases. All results are listed in Table 1. The column denoted "flag" indicates whether the fit is to flux *and* polarization (fp) or to the flux only (f). The last column illustrates the convergence properties in the multidimensional parameter space, referred to as success rate above (number of successful runs vs. total number of runs).

Model (A1), centred dipole viewed at $i = 60°$: the results in lines 1–4 assume $B^{\rm q}_{\rm pol} = 0$, those in lines 5–8 zero offset. All reconstructions are successful and reproduce the dipole field strength within 0.1 MG and the magnetic axis and the inclination with rms deviations of 5°and 8°, respectively. Not surprisingly, the accuracy of the reconstruction benefits from a high S/N, but is acceptable even for flux-only fits and a low S/N ratio. Note that errors in $\Phi^{\rm d}$ are irrelevant as long as $\Theta^{\rm d}$ matches closely. The same holds for $\Phi^{\rm q}$ and $\Theta^{\rm q}$ as long as $B^{\rm q}_{\rm pol}$ is close to zero. If all parameters are included in the fit (lines 9 and 10), a quadrupole component usually appears which is largely compensated for by a shift in the dipole (plus quadrupole) to the effect that the net field is dipole-like again. The low-noise flux-and-polarization fit of line 9 is quite acceptable, while the high-noise flux-only fit of line 10 produces larger misfits in i and in the field geometry. Even the latter provides an acceptable reconstruction over the visible part of the surface, but deviates strongly from the input in the permanently occulted part. This result is due to the inclusion of a higher multipole component than present in the input. Figure 10 demonstrates this result.

Model (A2), centred dipole viewed at $i = 30°$: the reconstructions are of a quality similar to that of model (A1). The permanently occulted fraction of the stellar surface, for which the reconstruction remains undefined, is now 25%.

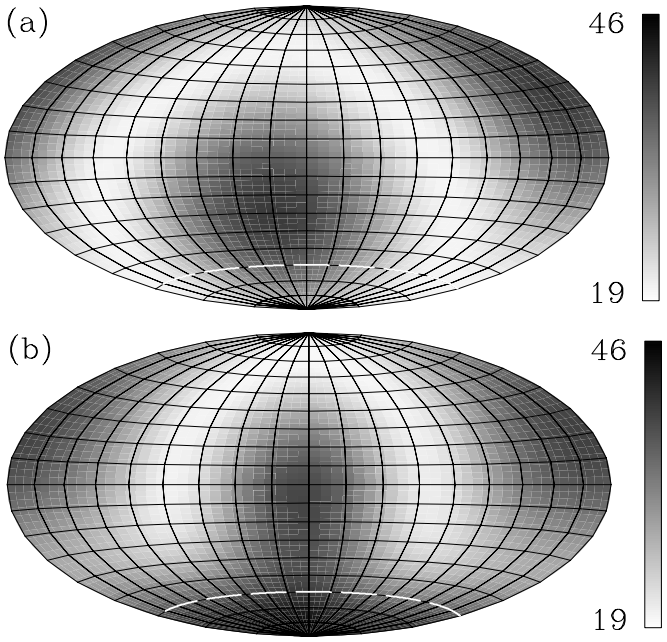

Fig. 10. Aitoff maps of the magnetic field strength B (in MG) for Model (A1). The input *(top)* and the high-noise flux-only reconstruction of Table 1, Model (A1), line 10 *(bottom)* are shown. The axis of the maps represents the rotation axis. The centre of the maps marks the $-x_0$ direction (see Fig. 2b). The region within 30° from the lower pole is permanently hidden (dashed white line).

Models (B, C), pure quadrupole and aligned dipole-quadrupole viewed at $i = 60°$: the four reconstructions each use the same set of parameters as lines 5–8 of model (A1). The lack of a dipole component in (B) and the relative strength of the dipole and quadrupole components in (C) are recognized even in the flux-only and high-noise fits.

Table 1. Reconstructed magnetic parameters for the configurations (A)–(F). Each model is introduced by a boldface line which lists the input parameters. The subsequent numbered lines represent the individual reconstructions. In the "flag" column, "fp" denotes simultaneous fits to flux and polarization spectra, "f" fits to flux spectra only. The last column indicates the success rate of the convergence of the multidimensional parameter search. Note that for (B) and (C), $\Theta^q = \Theta^d$ and $\Phi^q = \Phi^d$.

Model	i (°)	B^d_{pol} (MG)	Θ^d (°)	Φ^d (°)	B^q_{pol} (MG)	Θ^q (°)	Φ^q (°)	x'_{off} (R_{WD})	y'_{off} (R_{WD})	z'_{off} (R_{WD})	χ^2_{red}	S/N	flag	conv.
(A1), centred dipole viewed at $i = 60°$:														
	60.0	**40.0**	**60.0**	**340.0**	**0.0**	**0.0**	**0.0**	**0.0**	**0.0**	**0.0**	–	–	–	–
1	54.4	40.0	64.2	339.0	–	–	–	−0.001	0.000	0.000	1.07	100	fp	2/10
2	47.0	40.2	62.8	350.6	–	–	–	0.000	−0.001	−0.003	1.01	20	fp	2/10
3	55.3	40.3	64.1	339.6	–	–	–	0.007	0.000	−0.002	1.03	100	f	1/20
4	60.0	40.1	61.0	346.4	–	–	–	0.002	−0.002	0.002	0.94	20	f	6/20
5	63.0	40.0	57.4	340.7	−0.1	85.7	95.7	–	–	–	0.99	100	fp	7/20
6	70.6	40.2	49.9	345.2	−1.3	5.2	241.5	–	–	–	1.01	20	fp	13/20
7	62.3	39.9	57.1	339.7	0.0	23.2	265.3	–	–	–	1.02	100	f	2/6
8	45.5	40.0	66.0	358.0	0.5	23.5	228.6	–	–	–	1.00	20	f	2/6
9	56.2	39.8	63.9	339.6	−2.6	31.6	249.0	−0.013	−0.007	−0.004	1.02	100	fp	1/20
10	45.7	39.7	56.2	353.4	−20.9	38.8	179.8	0.075	0.001	−0.085	1.02	20	f	3/20
(A2), centred dipole viewed at $i = 30°$:														
	30.0	**40.0**	**60.0**	**340.0**	**0.0**	**0.0**	**0.0**	**0.0**	**0.0**	**0.0**	–	–	–	–
1	25.6	41.5	58.1	338.6	–	–	–	0.018	0.003	−0.014	1.03	100	fp	8/20
2	29.0	39.9	56.8	345.9	–	–	–	0.000	−0.006	−0.001	1.00	20	fp	9/20
3	29.5	39.5	59.0	339.6	−7.4	22.0	300.6	−0.068	−0.024	0.020	1.02	100	fp	1/20
(B), centred quadrupole viewed at $i = 60°$:														
	60.0	**0.0**	**60.0**	**340.0**	**40.0**	**60.0**	**340.0**	**0.0**	**0.0**	**0.0**	–	–	–	- -
1	56.7	0.1	63.0	339.9	40.0	63.0	339.9	–	–	–	0.97	100	fp	5/10
2	58.6	−0.8	60.8	331.2	40.0	60.8	331.2	–	–	–	1.02	20	fp	5/10
3	63.7	0.0	56.6	339.3	40.0	56.6	339.3	–	–	–	1.00	100	f	2/20
4	49.1	−0.4	61.7	346.2	40.0	61.7	346.2	–	–	–	1.00	20	f	5/20
(C), aligned centred dipole and quadrupole viewed at $i = 60°$:														
	60.0	**40.0**	**60.0**	**340.0**	**20.0**	**60.0**	**340.0**	**0.0**	**0.0**	**0.0**	–	–	–	–
1	58.8	40.0	61.3	340.1	20.1	61.3	340.1	–	–	–	0.93	100	fp	5/10
2	55.2	40.1	64.4	334.7	19.8	64.4	334.7	–	–	–	1.00	20	fp	5/10
3	58.5	40.0	64.8	340.6	20.1	64.8	340.6	–	–	–	1.05	100	f	3/20
4	51.1	40.0	65.4	338.3	20.0	65.4	338.3	–	–	–	0.99	20	f	9/20
(D), shifted high-field dipole viewed at $i = 60°$:														
	60.0	**110.0**	**0.0**	**0.0**	**0.0**	**0.0**	**0.0**	**0.05**	**−0.10**	**0.15**	–	–	–	–
1	60.1	110.1	0.3	150.2	–	–	–	0.051	−0.101	0.149	1.01	100	fp	1/10
2	61.1	109.7	0.3	223.6	–	–	–	0.056	−0.101	0.147	1.00	20	fp	3/10
3	59.8	109.9	0.1	218.1	–	–	–	0.050	−0.099	0.150	0.97	100	f	6/20
4	59.0	110.4	2.4	160.1	–	–	–	0.045	−0.105	0.154	1.05	20	f	1/20
5	59.8	109.8	0.1	90.1	−0.7	81.1	266.9	0.050	−0.100	0.150	0.99	100	fp	2/20
6	58.8	110.0	1.0	258.8	6.0	67.4	165.5	0.053	−0.105	0.162	0.93	20	f	18/20
(E), shifted dipole viewed at $i = 60°$:														
	60.0	**58.0**	**60.0**	**340.0**	**0.0**	**0.0**	**0.0**	**0.15**	**−0.10**	**0.30**	–	–	–	–
1	63.9	57.4	59.1	338.3	–	–	–	0.15	−0.09	0.30	1.02	100	fp	4/10
2	60.4	57.9	60.9	337.0	–	–	–	0.16	−0.08	0.30	1.05	20	fp	3/10
3	60.2	57.6	60.3	340.3	–	–	–	0.15	−0.10	0.30	1.04	100	f	10/20
4	56.4	59.1	61.3	341.0	–	–	–	0.16	−0.10	0.30	0.97	20	f	15/20
5	60.1	59.5	63.9	340.5	15.2	73.1	334.1	0.13	−0.09	0.23	1.06	100	fp	5/20
6	54.4	62.9	61.3	355.2	26.7	51.7	256.3	0.22	−0.16	0.29	1.00	20	f	11/20
(F), non-aligned dipole-quadrupole combination viewed at $i = 60°$:														
	60.0	**40.0**	**60.0**	**340.0**	**40.0**	**30.0**	**250.0**	**0.0**	**0.0**	**0.0**	–	–	–	–
1	58.8	40.3	58.5	337.3	39.8	31.9	247.3	–	–	–	1.01	100	fp	4/20
2	58.6	39.6	51.1	350.1	41.4	26.6	233.2	–	–	–	1.05	20	fp	10/20
3	66.2	39.9	68.0	347.4	40.4	26.7	270.0	–	–	–	1.13	100	f	5/20
4	43.3	49.1	51.2	273.6	−32.2	66.1	329.8	–	–	–	0.94	20	f	10/20
5	55.4	38.6	61.5	340.6	39.2	36.4	251.6	−0.022	0.009	−0.002	1.05	100	fp	1/20
6	46.7	39.4	36.7	269.9	30.4	39.0	248.8	0.051	0.078	−0.068	1.05	20	f	1/20

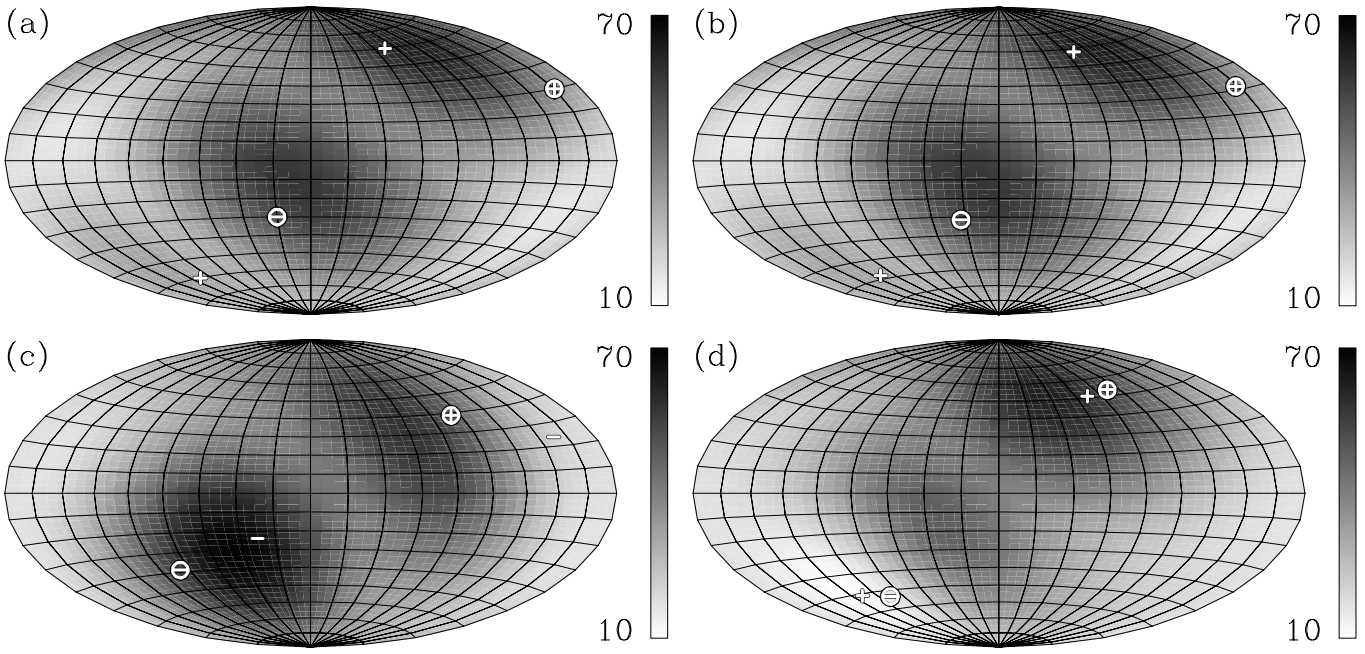

Fig. 11. Aitoff maps of the field strength B (in MG) showing the results of reconstruction fits for the Model (F) field distribution (non-aligned dipole-quadrupole combination). The centre of the maps marks the $-x_0$ direction. The axis of the quadrupole and the field direction at its poles is indicated by the + and − symbols, the axis of the dipole correspondingly by the circled + and − symbols (see text). **a)** Input field, **b)** low-noise flux-and-polarization reconstruction of Table 1, Model (F), line 1, **c)** high-noise flux-only reconstruction of line 4, and **d)** high-noise flux-only reconstruction of line 6.

Model (D), shifted high-field dipole viewed at $i = 60°$: the dipole is aligned with the rotation axis. Hence, the rotational modulation is caused by the off-centre shift. In spite of the weaker Zeeman structures (Fig. 6c, bottom), the configuration is recovered correctly if the search assumes a shifted dipole (lines 1–4). The absence of a quadrupole component is recognized in the low-noise flux-and-polarization fits (line 5), but less so in the high-noise flux-only fit (line 6). Interestingly, the offset is recognized correctly in both cases.

Model (E), shifted dipole viewed at $i = 60°$: this is the model which features one high-field spot. If modelled as a shifted dipole, the parameters are recovered with high accuracy, even when the S/N is low and the polarization is disregarded (lines 1–4). Allowing for a quadrupole component leads to the usual compensatory effects (lines 5 and 6). The reconstruction is acceptable over the visible surface, and deviates only slightly from the input field in the occulted part.

Model (F), non-aligned dipole-quadrupole combination viewed at $i = 60°$: all fits reproduce the general structure of the field with its two spots, separated by ∼90°, but only the fit using flux and polarization spectra at $S/N = 100$ (line 1) correctly finds the axes of both, the dipole and the quadrupole components. Convergence problems, which arise when the polarization is disregarded (line 3), may be due to a more corrugated χ^2-landscape compared with the fits including the polarization. Figure 11 provides an overview of the results for model (F). The input is depicted in Fig. 11a and the line-1 reconstruction in Fig. 11b. The high-noise flux-only fits of lines 4 and 6 (Figs. 11c and 11d) deviate in the strengths and orientations of the dipoles and quadrupoles. In Figs. 11a and 11b, the high-field spot on the northern (southern) hemisphere is dominated by the quadrupolar (dipolar) contribution. In Fig. 11c, the polarity of the quadrupole is reversed. Finally, in Fig. 11d, dipole and quadrupole are nearly aligned, but the spots are shifted due to the finite values of $x'_{\rm off}$ and $y'_{\rm off}$. Nevertheless, these fits are not altogether wrong if only the two-spot structure is considered. They suggest that a low $\chi^2_{\rm red}$ does, in fact, indicate a representation which bears some similarity to the input field structure, even if the choice of multipoles differs from that of the input. Seemingly, better results cannot be expected given the high noise of these two fits.

In summary, the code is able to reconstruct the magnetic field geometries of the type discussed here from phase-resolved flux and polarization spectra of high S/N. Our experience is that the inclusion of more than four phases does not improve the fits substantially, which is understandable given the overlap in surface coverage. Naturally, the reconstruction becomes less perfect when the polarization information is excluded and the noise is increased. Leaving off the polarization also seems to create convergence problems. An important aspect is that phase-dependent spectra allow the inclination of the rotation axis to be determined along with the field geometry. The accuracy achieved ranges from a few degrees to about 20° depending on the quality of the spectra.

5.3.3. Fits to a single spectrum

If only a single set of flux and polarization spectra or a single flux spectrum is available, information on the field distribution is reduced to the visible hemisphere. The location of the rotation axis remains unknown, and only the angle between the magnetic axis and the line of sight is constrained by the fit.

We have performed similar tests as above to single sets of spectra and find that simple field geometries can still be recovered.

6. Discussion

We have presented a formalized approach to the interpretation of phase-resolved flux and circular polarization spectra of rotating magnetic white dwarfs (MWDs). Tomographically locating positions with a certain field strength $\boldsymbol{B}$ on the surface of the star is hampered by the fact that only the self-eclipse of such a region manifests itself in flux spectra, while the positional information contributed by the rotation is obliterated by the Stark broadening.

6.1. Present approach

In our approach, we determine the parameters of a global field model directly by a least-squares fit to the spectral data. We caution that it is not a priori clear to what extent the global field can be constrained by such an approach, because the spectral information represents an average over the visible hemisphere at each phase. Our results demonstrate, however, that the phase-resolved Zeeman spectra contain enough information to allow the reconstruction of the field geometries considered by us. These involve combinations of dipoles and quadrupoles which are allowed to have different axes and to be shifted off-centre. The model contains up to ten free parameters and is sufficiently general to allow for rather complex surface field geometries featuring, e.g., a dominant single high-field spot, two spots separated by much less than 180°, or even a bipolar spot on an otherwise low-field star (not included in the models presented here). An advantage of our approach is that these fields automatically fulfil the requirement of being produced by sources inside the star. A disadvantage is the limitation in the number of free parameters.

In addition to the cases presented here, we have also attempted to reconstruct octupolar fields and were successful for aligned dipole-quadrupole-octupole combinations. However, if all multipole components with $l = 3$ and $m = 0, \ldots, 3$ are included (15 parameters for the expansion, two angles describing the direction of the reference axis, and the inclination), the `evoC` minimization algorithm encounters convergence problems, caused by too large a number of free parameters.

Another important aspect is the level of the signal-to-noise ratio S/N required for a successful reconstruction of the field. The model atmospheres of hydrogen-rich MWDs are characterized by the rather broad and strong Zeeman-shifted Balmer lines which allow a field reconstruction already for $S/N = 20$–100: $S/N = 20$ is the lower limit, while there is little improvement for $S/N > 100$. For comparison, Zeeman-Doppler imaging of main sequence stars operates on much fainter metal lines and needs a much higher S/N (Brown et al. 1991). However, while Zeeman-Doppler imaging is performed over individual lines, the high field strengths of the MWDs require a fit over the whole visible wavelength range.

In the analysis of observed Zeeman spectra, one may encounter some problems which are absent in the present reconstruction of synthetic spectra. While the variation of the statistical noise amplitude with wavelength can be accounted for in the χ^2-statistic (Eq. (13)), systematic uncertainties between the observed and calculated spectra cannot: (i) errors in the theoretical database spectra; and (ii) errors in the flux calibration of the observed spectra. Errors of type (i) may prevent a satisfactory convergence of the fits and/or lead to incorrect values of the parameters describing the field. Our experience is that such errors are of minor importance, given the present state of the theory of radiative transfer in magnetic stellar atmospheres. Errors of type (ii) may affect the ability to recognize high field spots on stars with a predominantly moderate field. For example, in model (F) at phase $\phi = 0.25$, and similarly in other models, the Hα σ^- component consists of a shallow depression extending from 5000 to 6000 Å. An error in the flux calibration which happens to weaken or strengthen such a depression can lead to serious errors in the derived field distribution. A careful flux calibration is, therefore, of utmost importance.

6.2. Different optimization strategies

Should MWDs turn out to have field geometries which are more complex and require more free parameters than adopted by us, we may have to consider alternative optimization techniques. E.g., a genetic algorithm may be more robust than the `evoC` code and allow for a somewhat larger number of parameters. A full harmonic expansion with $l \gg 2$ may become tractable if a regularization operator like MEM drives the solution towards low-order fields while permitting higher-order components to be used as necessary to fit the data.

6.3. The ZEBRA approach

The problem of retrieving the field structure of rotating MWDs has previously been studied by Donati et al. (1994) in what they called the ZEBRA approach. They used a maximum-entropy method to deduce the most likely two-dimensional frequency distribution $f(B_\mathrm{t}, B_\mathrm{l})$ of the transverse and longitudinal field components with respect to the line of sight separately for each rotational phase. The method has the obvious advantage that no a priori assumption is made about the global field structure. On the other hand, the interrelation between the overlapping field distributions at different rotational phases is not utilized and there is no prescription for the interpretation of such an interrelation in terms of a global field. Indeed, there is no guarantee of a physically meaningful reconstruction (e.g. sources only within the star leading to a curl-free field outside the star). Thus, the detailed structure and the physical characteristics of the global field remain undefined in the ZEBRA method in the present form (Donati et al. 1994).

If the underlying global field structure is sufficiently simple, it may be derived in a second step added to the ZEBRA method. In a first step, the best-fit ZEBRA diagrams (or B–ψ diagrams similar to ours) are determined using a MEM-type regularization scheme as suggested by Donati et al. (1994). In a second step, a parametrized global magnetic field model is then fitted to the phase-resolved ZEBRA diagrams.

Since the second step would not involve the computation of spectra from the database, which is by far the most time-critical process in the present method, this two-step approach is probably advantageous with respect to CPU time. Without detailed tests, however, it is not clear whether this approach would be superior to directly fitting the Zeeman spectra.

6.4. A future approach

One may endeavour to relax the restrictions on the global field structure by parametrizing the surface field as $(\boldsymbol{B}_1, \ldots, \boldsymbol{B}_N)$ for a star with N surface elements and to impose a regularization scheme, e.g. MEM, to ensure the smoothness of the solution. The feasibility of such an approach, its convergence properties, and the interpretation of the derived field model would still have to be studied, however, as well as the demands on computation time given the formidable number of parameters.

7. Conclusion

We have described a method to reconstruct the field structure of magnetic white dwarfs which provides an internally consistent fit to spectropolarimetric data taken at different rotational phases in terms of a parametrized field model. We presently use dipoles and quadrupoles which are allowed to be shifted off-centre to increase the versatility of the model. An application to real data will be described elsewhere.

We do not know whether MWDs have the regular fields adopted here or possibly field structures as complex as spotted main sequence stars. Fortunately, there are several single white dwarfs with known rotational periods, and about 60 rotating MWDs in cataclysmic binaries, some of which are known to have fields which deviate from simple centred dipoles. The study of such systems using the present and similar techniques promises to increase our knowledge of the end-product of magnetic stellar evolution.

Acknowledgements. We thank Torsten Rahn for his contributions to the Kiel fraction of this program and Klaus Reinsch for fruitful discussions. FE acknowledges a grant from Graduiertenförderung des Landes Niedersachsen. This work was supported in part by BMBF/DLR grant 50 OR 9903 6.

References

Beckers, J. M. 1969, Sol. Phys., 9, 372
Brown, S. F., Donati, J.-F., Rees, D. E., & Semel, M. 1991, A&A, 250, 463
Burleigh, M. R., Jordan, S., & Schweizer, W. 1999, ApJ, 510, L37
Dittmann, O. 1995, Dissertation, Heidelberg
Donati, J.-F., Achilleos, N., Matthews, J. M., & Wesemael, F. 1994, A&A, 285, 285
Donati, J.-F., Semel, M., & Praderie, F. 1989, A&A, 225, 467
Euchner, F. 1998, Diplomarbeit, Georg-August-Universität Göttingen
Forster, H., Strupat, W., Rösner, W., et al. 1984, J. Phys. V, 17, 1301
Gänsicke, B. T., & Beuermann, K. 1996, A&A, 309, L47
Gänsicke, B. T., Hoard, D. W., Beuermann, K., Sion, E. M., & Szkody, P. 1998, A&A, 338, 933
Hardorp, J., Shore, S. N., & Wittmann, A. 1976, in Physics of Ap stars, ed. W. W. Weiss, H. Jenkner, & H. J. Wood, IAU Coll., 32, 419
Jordan, S. 1992, A&A, 265, 570
Jordan, S. 2001, in 12th European Workshop on White Dwarfs, ed. J. L. Provencal, H. L. Shipman, J. MacDonald, & S. Goodchild (San Francisco: Astronomical Society of the Pacific), ASP Conf. Ser., 226, 269
Jordan, S., & Merani, N. 1995, in 9th European Workshop on White Dwarfs, ed. D. Koester, & K. Werner (Berlin: Springer Verlag), Lect. Notes in Phys., 443, 134
Koester, D., Schulz, H., & Weidemann, V. 1979, A&A, 76, 262
Kube, J., Gänsicke, B. T., & Beuermann, K. 2000, A&A, 356, 490
Lamb, F. K., & Sutherland, P. G. 1974, in Physics of Dense Matter, ed. C. J. Hansen (Dordrecht: Reidel), IAU Symp., 53, 265
Langel, R. A. 1987, in Geomagnetism, ed. J. A. Jacobs, vol. 1 (London: Academic Press), 249
Merani, N., Main, J., & Wunner, G. 1995, in Astrophysical Applications of Powerful New Databases, ed. S. J. Adelman, & W. L. Wiese (San Francisco: Astronomical Society of the Pacific), ASP Conf. Ser., 78, 81
Muslimov, A. G., Van Horn, H. M., & Wood, M. A. 1995, ApJ, 442, 758
Nelder, J. A., & Mead, R. 1965, Comp. J., 7, 308
Press, W. H., Teukolsky, S. A., Vetterling, W. T., & Flannery, B. P. 1992, Numerical Recipes in C, 2nd ed. (Cambridge University Press)
Putney, A., & Jordan, S. 1995, ApJ, 449, 863
Rahn, T. 1999, Diplomarbeit, Christian-Albrechts-Universität Kiel
Ramaty, R. 1969, ApJ, 158, 753
Rechenberg, I. 1994, Evolutionsstrategie '94, Werkstatt Bionik und Evolutionstechnik, 1 (Stuttgart: frommann-holzboog)
Rösner, W., Wunner, G., Herold, H., & Ruder, H. 1984, J. Phys. V, 17, 29
Schwope, A. D. 1995, Rev. Mod. Astron., 8, 125
Semel, M. 1989, A&A, 225, 456
Takeda, Y. 1991, PASJ, 43, 719
Trint, K., & Utecht, U. 1994, `ftp://ftp-bionik.fb10.tu-berlin.de/pub/software/evoC/`
Unno, W. 1956, PASJ, 8, 108
Wickramasinghe, D. T., & Cropper, M. 1988, MNRAS, 235, 1451
Wickramasinghe, D. T., & Ferrario, L. 2000, PASP, 112, 873
Wickramasinghe, D. T., & Martin, B. 1979, MNRAS, 189, 883
Wunner, G., Rösner, W., Herold, H., & Ruder, H. 1985, A&A, 149, 102